J. Fluid Mech. (2024), *vol*. 993, R3, doi:10.1017/jfm.2024.630

Heat transport in liquid metal convection from onset to turbulence: the effect of small aspect ratio

Lei Ren[1], **Xin Tao**[1], **Lu Zhang**[2,3], **Ke-Qing Xia**[2,3,4] **and Yi-Chao Xie**[1,†]

[1]State Key Laboratory for Strength and Vibration of Mechanical Structures, School of Aerospace, Xi'an Jiaotong University, Xi'an 710049, PR China

[2]Centre for Complex Flows and Soft Matter Research, Southern University of Science and Technology, Shenzhen 518055, PR China

[3]Department of Mechanics and Aerospace Engineering, Southern University of Science and Technology, Shenzhen 518055, PR China

[4]Department of Physics, Southern University of Science and Technology, Shenzhen 518055, PR China

(Received 14 May 2024; revised 16 July 2024; accepted 16 July 2024)

We present a systematic study on the effects of small aspect ratios Γ on heat transport in liquid metal convection with a Prandtl number of $Pr = 0.029$. The study covers $1/20 \leq \Gamma \leq 1$ experimentally and $1/50 \leq \Gamma \leq 1$ numerically, and a Rayleigh number Ra range of $4 \times 10^3 \leq Ra \leq 7 \times 10^9$. It is found experimentally that the local effective heat transport scaling exponent γ changes with both Ra and Γ, attaining a Γ-dependent maximum value before transition-to-turbulence and approaches $\gamma = 0.25$ in the turbulence state as Ra increases. Just above the onset of convection, Shishkina (*Phys. Rev. Fluids*, vol 6, 2021, 090502) derived a length scale $\ell = H/(1 + 1.49\Gamma^{-2})^{1/3}$. Our numerical study shows Ra_ℓ, i.e. Ra based on ℓ, serves as a proper control parameter for heat transport above the onset with $Nu - 1 = 0.018(1 + 0.34/\Gamma^2)(Ra/Ra_{c,\Gamma} - 1)$. Here $Ra_{c,\Gamma}$ represents the Γ-dependent critical Ra for the onset of convection and Nu is the Nusselt number. In the turbulent state, for a general scaling law of $Nu - 1 \sim Ra^\alpha$, we propose a length scale $\ell = H/(1 + 1.49\Gamma^{-2})^{1/[3(1-\alpha)]}$. In the case of turbulent liquid metal convection with $\alpha = 1/4$, our measurement shows that the heat transport will become weakly dependent on Γ with $Ra_\ell \equiv Ra/(1 + 1.49\Gamma^{-2})^{4/3} \geq 7 \times 10^5$. Finally, once the flow becomes time-dependent, the growth rate of Nu with Ra declines compared with the linear growth rate in the convection state. A hysteresis is observed in a $\Gamma = 1/3$ cell when the flow becomes time-dependent. Measurements of the large-scale circulation suggest the

† Email address for correspondence: yichao.xie@xjtu.edu.cn

hysteresis is caused by the system switching from a single-roll-mode to a double-roll-mode in an oscillation state.

Key words: Bénard convection, turbulent convection

1. Introduction

Thermal convection in liquid metal occurs widely in geophysical, astrophysical systems and industrial processes (Lohse & Shishkina 2023), such as the outer core of the Earth (King & Aurnou 2013) and blanket design of nuclear fusion reactors (Salavy *et al.* 2007). The most salient feature of liquid metal is its Prandtl number $Pr = \nu/\kappa$ being much smaller than unity, resulting in faster diffusion of heat than momentum. Here, ν and κ are the fluid's kinematic viscosity and thermal diffusivity, respectively. To study the various thermal convection phenomena, the Rayleigh–Bénard convection (RBC) system is usually employed (for reviews, see e.g. Ahlers, Grossmann & Lohse 2009; Lohse & Xia 2010; Chillá & Schumacher 2012; Xia 2013). In RBC, a horizontally infinite fluid layer confined between two plates is heated from below and cooled from above. This system is governed by two control parameters, namely, the Rayleigh number $Ra = \alpha g \Delta T H^3/(\nu\kappa)$ and Pr, where α, ΔT and g denote the thermal expansion coefficient, the applied temperature difference across the fluid layer and the gravitational acceleration constant, respectively. In addition, the aspect ratio $\Gamma = D/H$ for a given cell geometry is used to characterize the effect of spatial confinement with H and D being the height and diameter for a cylindrical cell. Understanding the heat transport mechanism remains one of the central issues in the study of thermal convection. Much progress has been made regarding heat transport in fluids like water/air with $Pr \sim O(1)$. A great success is the good agreement of the Nusselt number Nu between the prediction of the theory proposed by Grossmann & Lohse (Grossmann & Lohse 2000; Stevens *et al.* 2013) (GL theory) and various experimental and numerical measurements in cells with $\Gamma \sim 1$ (see, e.g. Ahlers *et al.* 2009, and references therein). Here, the Nu number characterizes the ratio between the heat flux transported by the system to that by thermal conduction alone, which is usually expressed in terms of a power law with Ra, i.e. $Nu \sim Ra^{\alpha}$.

As a sidewall is unavoidable in experimental set-ups, Γ for a given cell geometry is also important. Owing to the demand for achieving, as large as possible, the Ra for a given D, slender cells with $\Gamma < 1$ are usually preferred. For the onset of convection, Shishkina (2021) theoretically showed that the critical Rayleigh number for the onset of convection is $Ra_{c,\Gamma} = (2\pi)^4(1 + 1.49/\Gamma^2)(1 + 0.34/\Gamma^2)$, and the heat transport just above the onset of convection is predicted to be $Nu - 1 \sim (1 + 1.49/\Gamma^2)^{-1}Ra$. Experimental measurements of $Ra_{c,\Gamma}$ have confirmed the above Γ-dependence of Ra_c (Zhang & Xia 2023; Ren *et al.* 2024). However, the predicted heat transport relation has yet not been tested. In the turbulent state, studies on the effects of $\Gamma < 1$ mainly focus on fluids with $Pr \sim 4.3$. Two-dimensional direct numerical simulation (DNS) shows that small Γ has more profound influences on the heat transport in fluids with $Pr = 0.7$ when compared with that with $Pr = 4.3$ (Van der Poel, Stevens & Lohse 2011). In rectangular cells, it is shown that reducing Γ in one direction leads to the condensation of coherent structures and the emergence of an optimal heat transport state (Huang *et al.* 2013; Xia *et al.* 2023). In cylindrical cells, the heat transport depends weakly on Γ with the maximum difference being $\sim 2\,\%$ for $4 \times 10^9 \leq Ra \leq 10^{11}$ in cells with $1/3 \leq \Gamma \leq 1$ (Xi & Xia 2008; Weiss & Ahlers 2011), despite that the large-scale circulation (LSC) changes from a

double-roll-mode (DRM) dominated state to a single-roll-mode (SRM) dominated state when Γ changes from 1/3 to 1. The insensitive heat transport to the LSC mode is partially due to the thermal boundary layer (BL) being protected by the viscous BL in fluids with $Pr > 1$. Thus, the changes in the LSC mode cannot directly impact the thermal BL that controls the heat transport efficiency.

Compared with the large body of knowledge accumulated on the effects of small Γ in working fluids with $Pr \geq 0.7$, studies on the effects of small Γ in liquid metal convection with $Pr \sim 10^{-2}$ remain scarce. Early studies in liquid metal convection mainly focus on the regime with $\Gamma \geq 1$ and found that $Nu \sim Ra^{0.25}$ (Rossby 1969; Takeshita *et al.* 1996; Cioni, Ciliberto & Sommeria 1997; Horanyi, Krebs & Müller 1999; Aurnou & Olson 2001; King & Aurnou 2013; Scheel & Schumacher 2016; Zürner *et al.* 2019; Ren *et al.* 2022). In cells with $\Gamma = 1$ and 1/2, it is found that the LSC exhibits different structures depending on the cell geometry and the Ra range. For example, in a $\Gamma = 1/2$ cuboid cell for $10^5 < Ra < 10^7$, the LSC evolves from a twisted LSC state to a LSC state, and the heat transport of the latter is approximately 35 % larger than that of the former when they coexist (Chen *et al.* 2023). The SRM LSC usually observed in cylindrical cells with $\Gamma = 1$ are found to collapse in a cell with $\Gamma = 1/2$ when $Ra > 2 \times 10^8$ (Schindler *et al.* 2022). After a correction to the experimental data first published in Schindler *et al.* (2022), the heat transport in the $\Gamma = 1/2$ cell is found to be systematically larger (up to 30 %) than that in the $\Gamma = 1$ cell (Schindler *et al.* 2023). For even smaller Pr, i.e. liquid sodium with $Pr \sim 0.009$, the heat transport scaling α is found to depend strongly on Γ, i.e. $\alpha = 0.40$ in a $\Gamma = 1/5$ cell for $6.50 \times 10^8 \leq Ra \leq 1.25 \times 10^9$ (Frick *et al.* 2015) and $\alpha = 0.76$ in a $\Gamma = 1/20$ cell for $2.02 \times 10^{10} \leq Ra \leq 4.56 \times 10^{10}$ (Mamykin *et al.* 2015), highlighting the significance of Pr on heat transport in slender cells. Apart from heat transport, it is also found that spatial confinement facilitates the transition to turbulence in liquid metal convection due to the formation of multiple vertically stacked rolls and frequent transitions between them in the small Γ regime (Ren *et al.* 2024). The above analysis suggests our understanding of the effects of $\Gamma < 1$ on heat transport in liquid metal convection remains incomplete, which motivates the present study.

In this paper, combing experimental measurements and DNS, we will show that just above the onset of convection, in the range of $1/50 \leq \Gamma \leq 1$, the Nu grows linearly with Ra with $Nu - 1 = 0.018(1 + 0.34/\Gamma^2)(Ra/Ra_{c,\Gamma} - 1)$. If the flow becomes time-dependent when Ra increases beyond $Ra_{c,\Gamma}$, the slope of the linear growth will decline. Extending the theory by Shishkina (2021), we propose a length scale in the turbulent state, i.e. $\ell = H/(1 + 1.49\Gamma^{-2})^{1/[3(1-\alpha)]}$. We will show that once this new length scale is employed, the heat transport efficiency in turbulent liquid metal convection with $\alpha = 1/4$ in cells with $1/3 \leq \Gamma \leq 1$ will collapse for $Ra_\ell \geq 7 \times 10^5$.

2. The experimental and numerical set-ups

2.1. *The experiments*

The experiments were carried out in cylindrical convection cells with the aspect ratio varied in the range of $1/20 \leq \Gamma \leq 1$ and the Ra in a range of $4 \times 10^3 \leq Ra \leq 7 \times 10^8$. To achieve such a wide range of Ra, three sets of cells with diameter $D = 20.14$ mm, 40.37 mm and 103.91 mm were constructed. They are referred to as sets A, B and C, respectively. Figure 1(*a*) shows the range of Γ and Ra for each set of cells. To vary Γ for each set, sidewalls with respective height H corresponding to the designed Γ were used. In total 11 convection cells were used. The design and construction of the cells

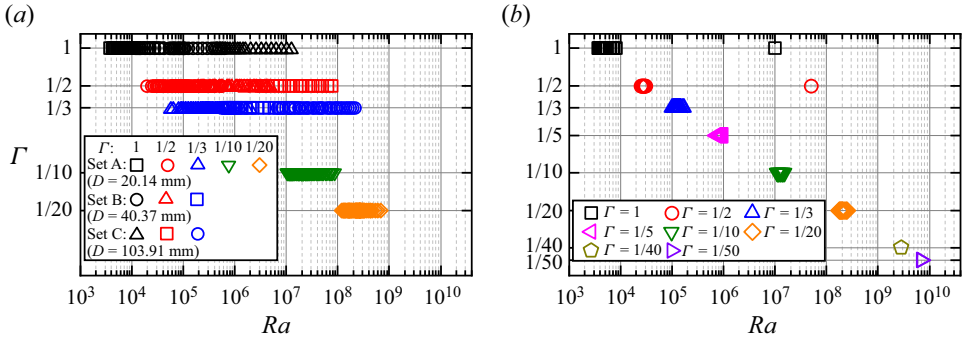

Figure 1. The $\Gamma - Ra$ parameter space for (a) experiments and (b) DNS with $Pr = 0.029$.

are similar and can be found in Ren *et al.* (2022). We mention here only their essential features. Each convection cell consists of a top cooling copper plate, a bottom heating copper plate and a Plexiglas sidewall. The surface facing the fluid is coated with a thin layer of nickel. The Plexiglas sidewall was sandwiched between the two copper plates. A fluorine rubber O-ring was employed between the ends of the sidewall and the plates to prevent the leakage of gallium–indium–tin (GaInSn). The bottom plate was heated by a nichrome wire heater, while the top plate was cooled by circulating temperature-controlled water. The temperature boundary condition at the bottom plate is a constant heat flux and that of the top plate is a constant temperature, nominally. The respective temperatures of the top (bottom) plate were measured using four (five) thermistors inserted into blind holes drilled from their sides with a distance of 3 mm from the plate–fluid interface. A digital multimeter was used to measure the resistance of the thermistors, which were then converted to temperatures using calibrated parameters. The sampling rate of the temperature measurement is 0.35 Hz. By measuring the voltage V and current I applied to the heater using a four-wire method, the applied time-averaged heat flux $q = 4VI/(\pi D^2)$ and thus the $Nu = qH/(\chi \Delta T)$ can be obtained. Here $\chi = 24.9$ W (mK)$^{-1}$ is the thermal conductivity of GaInSn. The experimental conditions of sets A and B can be found in the appendix of Ren *et al.* (2024). For the set C cells, ΔT varies in the range of [0.48, 23.69] K and [0.61, 19.54] K for $\Gamma = 1/2$ and 1/3, respectively. For high-precision heat transport measurements, side and bottom temperature-controlled thermal shields were installed. We refer to Ren *et al.* (2022) for more details on the experimental procedure. The liquid metal alloy GaInSn was used as the working fluid. Its physical properties are documented in Ren *et al.* (2022). Its Pr was fixed at $Pr = 0.029$ with a mean fluid temperature of 35 °C.

2.2. *Direct numerical simulations*

Direct numerical simulations were conducted in a cylindrical domain with $1/50 \leq \Gamma \leq 1$ and in the Ra range of $3.7 \times 10^3 \leq Ra \leq 6.9 \times 10^9$. Figure 1($b$) shows the range of Γ and Ra for DNS. The non-dimensional governing equations with the Oberbeck–Boussinesq approximation, cf. (2.1), were numerically solved using a fourth-order finite-volume method on staggered grids, and the time marching is done using the Euler-leapfrog scheme (Chong, Ding & Xia 2018),

$$\frac{\partial \boldsymbol{u}}{\partial t} + (\boldsymbol{u}\cdot\boldsymbol{\nabla})\boldsymbol{u} = -\boldsymbol{\nabla} p + \sqrt{\frac{Pr}{Ra}}\nabla^2\boldsymbol{u} + T\hat{\boldsymbol{z}}; \quad \frac{\partial T}{\partial t} + (\boldsymbol{u}\cdot\boldsymbol{\nabla})T = \sqrt{\frac{1}{RaPr}}\nabla^2 T; \quad \boldsymbol{\nabla}\cdot\boldsymbol{u} = 0, \tag{2.1}$$

where $\boldsymbol{u}$, T and p are, respectively, the dimensionless velocity, temperature and pressure; $\hat{\boldsymbol{e}}_z$ is the unit vector in the vertical direction. Equations (2.1) have been made dimensionless using the cell height H, the temperature difference across the cell ΔT, the free-fall velocity $u_{ff} = \sqrt{\alpha g \Delta T H}$ and the free-fall time scale $\tau_{ff} = H/u_{ff}$. All boundaries satisfy the no-penetration and no-slip velocity boundary conditions. The top/bottom plates are kept isothermal and the sidewalls are kept adiabatic.

The accuracy of the DNS is verified through the two well-known exact relations in RBC (Ahlers *et al.* 2009), i.e. $Nu = Nu_{\epsilon_u} = Nu_{\epsilon_T}$. Here $Nu = 1 + \sqrt{RaPr}\,\langle u_z T\rangle_{V,t}$, $Nu_{\varepsilon_u} = 1 + \sqrt{RaPr}\,\langle \varepsilon_u\rangle_{V,t}$ and $Nu_{\varepsilon_T} = \sqrt{RaPr}\,\langle \varepsilon_T\rangle_{V,t}$, where $\langle\cdots\rangle_{V,t}$ denotes averaging over the entire simulation domain and the statistical time. Here Nu, Nu_{ε_u} and Nu_{ε_T} are the directly calculated Nusselt number, the Nusselt number calculated based on the viscous dissipation rate ε_u and the thermal dissipation rate ε_T, respectively. For simulations just above the onset of convection, the difference between three Nu values is within 0.1 %, and that of the turbulent state is within 4 %. Each simulation case was started from a state with a linear temperature profile and zero velocity plus a small perturbation. Details of the simulation can be found in the Appendix.

3. Results and discussions

3.1. *General features of the heat transport*

We first take an overview of the heat transport data. Figure 2(*a*) plots Nu as a function of Ra obtained experimentally as open symbols and numerically as solid stars in cells with $1/20 \le \Gamma \le 1$. The green solid line marks the theoretical prediction of the GL theory for $\Gamma = 1$ (Grossmann & Lohse 2000) with modified prefactors taking into account new measurements at $Pr = 0.029$ from Ren *et al.* (2022). Firstly, it is seen that the experimentally measured Nu and the Nu obtained from DNS in a cell with $\Gamma = 1$ for $Ra = 10^7$ and in a cell with $\Gamma = 1/2$ for $Ra = 5 \times 10^7$ overlap with each other within ~ 3 %, suggesting that the finite conductivity effects (Verzicco 2004) in the studied parameter range is small. One also observes that the agreement between measurements and DNS data near the onset of convection is not good. This point will be discussed in § 3.2. For large enough Ra, Nu in cells with $1/3 \le \Gamma \le 1$ all approach the prediction of the GL theory, suggesting that the system will become Γ-independent when Ra is larger than a Γ-dependent critical value. This observation is different from the results reported by Schindler *et al.* (2023) within a similar range of Ra and the same Pr, where they observe a ~ 30 % difference in Nu between measurements in two cylindrical cells with $\Gamma = 1$ and 1/2 (see figure 5*c*).

We now study measurements in the $\Gamma = 1$ cells. Figure 2(*a*) shows that Nu numbers measured in three sets of cells overlap well with each other when there is an overlap in Ra. The flow evolves from the conduction state at $Ra \approx 5 \times 10^3$ to a turbulent state for $Ra > 10^5$. Let us denote the Nu measured experimentally in the conduction state as a_Γ. Note a_Γ should be 1, independent of Γ by definition. However, due to unknown parasitic heat leakage, figure 2(*a*) shows that a_Γ is slightly larger than 1 and increases with decreasing Γ. Before the transition-to-turbulence state, i.e. Ra smaller than the vertical dashed lines, which mark the critical Rayleigh number for the transition-to-turbulence state reported in Ren *et al.* (2022, 2024), the local effective heat transport scaling exponent γ of Nu versus Ra, i.e. $\gamma = \mathrm{d}\log Nu/\mathrm{d}\log Ra$, changes continuously, as shown in figure 2(*b*). Here γ is obtained by fitting the data using a sliding window covering approximately half a decade in Ra. In the turbulent state, we observe an $Nu \sim Ra^{0.25}$ scaling, in good agreement with the prediction of $\alpha = 1/4$ obtained from the GL theory (Grossmann & Lohse 2000),

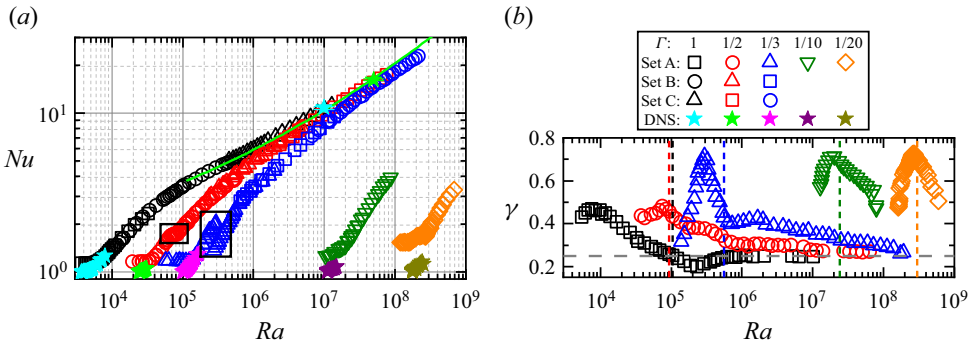

Figure 2. (*a*) Measured *Nu* versus *Ra* from experiments (open symbols) and DNS (solid symbols) for different Γ. The green solid line is the prediction of the GL theory with $\Gamma = 1$ (Grossmann & Lohse 2000). (*b*) The local effective heat transport scaling exponent γ versus *Ra*. The vertical dashed lines mark the transitional *Ra* when the system becomes turbulent.

experimental measurements (Cioni *et al.* 1997; Glazier *et al.* 1999; Zürner *et al.* 2019; Ren *et al.* 2022) and numerical simulations (Verzicco & Camussi 1997; Scheel & Schumacher 2016).

In the cells with $\Gamma = 1/2$ and $1/3$, the *Nu* measured in different sets of cells but the same Γ also overlap with each other when there is an overlap in *Ra*. The system starts from the conduction state and evolves into a turbulent state when *Ra* is larger than the critical values marked by the vertical dashed lines in figure 2(*b*). Similar to the case with $\Gamma = 1$, the local effective heat transport scaling exponent γ increases with *Ra* before the system becomes turbulent, and it decreases with *Ra* in the turbulent state. For sufficiently large *Ra*, γ approaches 0.25 as marked with a long-dashed horizontal line in figure 2(*b*).

In the strongly confined regime with $\Gamma = 1/10$ and $1/20$, the system starts from the conduction state and becomes turbulent very quickly after the onset of convection (Ren *et al.* 2024). The local effective heat transport scaling exponents γ show similar behaviour as those in cells with $1/3 \leq \Gamma \leq 1$, i.e. they increase to a maximum value γ_{max} and then start to decrease in the turbulent state. In these two cases, we observe $\gamma_{max} = 0.75$. We note that a similar observation, i.e. an increased local effective scaling exponent γ with decreasing Γ was reported in strongly confined rectangular cells with water ($Pr = 4.38$) as the working fluid (Zhang & Xia 2023). However, the γ in water is much larger than in the present study with liquid metal. For example, Zhang & Xia (2023) reported $\gamma_{max} = 4.30$ and 8.49 from the experiment and DNS in a cell with $\Gamma = 1/20$, respectively. The difference may be attributed to the difference in *Pr* or the cell geometry, highlighting the sensitive dependence of the heat transport on the control parameters and cell geometry in the severely confined RBC. Finally, we note that there are discontinuities in the $Nu \sim Ra$ curve beyond the onset of convection in cells with $\Gamma = 1/2$ and 1/3, marked by the two black rectangles in figure 2(*a*). The reason for the discontinuities will be discussed in § 3.3.

3.2. *Length scale in confined turbulent RBC*

Shishkina (2021) predicts that near the onset of convection, the heat transport is

$$Nu - 1 = C(1 + c_u \Gamma^{-2})^{-1} Ra \tag{3.1}$$

with $c_u = 1.49$ and C being a undetermined prefactor. Thus, the relevant length scale near the onset of convection is $\ell = H/(1 + c_u\Gamma^{-2})^{1/3}$. Assuming there is a power law relation between Nu and Ra, i.e. $Nu - 1 \sim Ra^{\alpha}$, following Shishkina (2021), let us define a function $f \equiv (Nu - 1)Ra^{-\alpha}$. Then (3.1) transforms into

$$f \equiv (Nu - 1)Ra^{-\alpha} \sim \left[\frac{Ra}{(1 + c_u\Gamma^{-2})^{1/(1-\alpha)}}\right]^{1-\alpha}. \tag{3.2}$$

In the classical turbulent regime, the heat transport scaling $Nu - 1 \sim Ra^{\alpha}$ holds with the scaling exponent α depending on the flow regime (Grossmann & Lohse 2000) but weakly depend on Γ. Following Shishkina (2021), we further assume that the expression inside the square bracket of (3.2) near the onset of convection also holds in the classical turbulent regime and denote it as Ra_ℓ. We then obtain a α-dependent length scale $\ell = H/[(1 + c_u\Gamma^{-2})^{1/[3(1-\alpha)]}]$. For turbulent liquid metal convection, our measurements in cells with $1/3 \leq \Gamma \leq 1$ (see figure 2*b*) and previous studies in cells with $\Gamma = 1$ (Takeshita *et al.* 1996; Cioni *et al.* 1997; Glazier *et al.* 1999; King & Aurnou 2013; Zürner *et al.* 2019; Ren *et al.* 2022) suggest α approaches 1/4 with increasing Ra, which is also predicted by GL theory for small Pr and not too large Ra (Grossmann & Lohse 2000). Plugin $\alpha = 1/4$ into ℓ and Ra_ℓ, we have

$$\ell = H/(1 + c_u\Gamma^{-2})^{4/9} \quad Ra_\ell \equiv Ra/(1 + c_u\Gamma^{-2})^{4/3}, \tag{3.3}$$

for turbulent liquid metal convection. We are now in a position to test the above length scales using the heat transport data just above the onset of convection and in the turbulent state. As we will show next, (3.1) and (3.3) hold near the onset of convection and in the turbulent state in liquid metal convection, respectively, suggesting that the proposed length scales are justified.

Just above the onset of convection, the experimentally measured Nu is not accurate (see figure 2*a*) due to unknown parasitic heat leakage. Thus, the following discussion about heat transport just above the onset of convection is mainly based on the DNS data. Details of the DNS data just above the onset of convection can be found in the Appendix.

Figure 3(*a*) plots $Nu - 1$ versus $Ra/Ra_{c,\Gamma} - 1$ just above the onset of convection obtained numerically. Here $Ra_{c,\Gamma}$ is the Γ-dependant critical Rayleigh number for the onset of convection reported in Ren *et al.* (2024). The horizontal grey dashed line marks $Nu - 1 = 0$, i.e. the conduction state. A linear function, i.e. $Nu - 1 = A(Ra/Ra_c - 1)$, is used to fit the data for different Γ with the fitting results shown as solid lines in the figure. It is seen that with decreasing Γ, the slope of the linear curve becomes larger, suggesting a steeper growth of Nu with $Ra/Ra_{c,\Gamma}$ for smaller Γ. Figure 3(*b*) shows $(Nu - 1)/A$ versus $Ra/Ra_{c,\Gamma} - 1$. It is seen that data for different Γ now collapse onto a single master curve with a slope of 1, suggesting that the proposed length scale near the onset of convection, i.e. $\ell = H/(1 + c_u\Gamma^{-2})^{1/3}$, is justified. The fitted coefficient A versus Γ is shown in figure 3(*c*). A fitting function in the form of $A = C(1 + 0.34/\Gamma^2)$ as proposed by Shishkina (2021) is used to fit the coefficient A obtained from DNS data, from which we obtain $C = 0.018 \pm 0.01$. Thus, the heat transport just above the onset of convection follows $Nu - 1 = 0.018(1 + 0.34/\Gamma^2)(Ra/Ra_{c,\Gamma} - 1)$. The inset of figure 3(*c*) plots A versus $1/\Gamma^2$, which now becomes a straight line. It is seen that the numerically obtained A is in good agreement with the fitting curve.

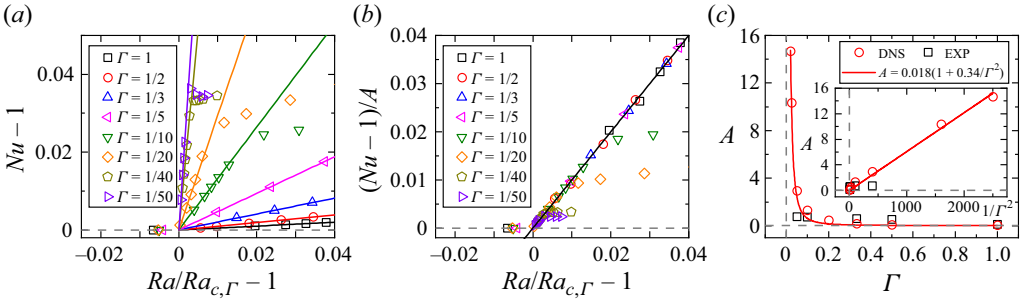

Figure 3. Numerically obtained heat transport just above the onset of convection. (*a*) Here, $Nu - 1$ versus $Ra/Ra_{c,\Gamma} - 1$. The horizontal dashed line marks the conduction state. The solid lines are linear fitting to the data just above the onset of convection, i.e. $Nu - 1 = A(Ra/Ra_{c,\Gamma} - 1)$. (*b*) Here, $(Nu - 1)/A$ versus $Ra/Ra_{c,\Gamma} - 1$. (*c*) The prefactor A of the linear fitting versus Γ. Red circles and black squares represent the DNS and experimental (EXP) data, respectively. The red solid line is a fit of $A = 0.018(1 + 0.34/\Gamma^2)$ to the DNS data. The inset shows A versus $1/\Gamma^2$.

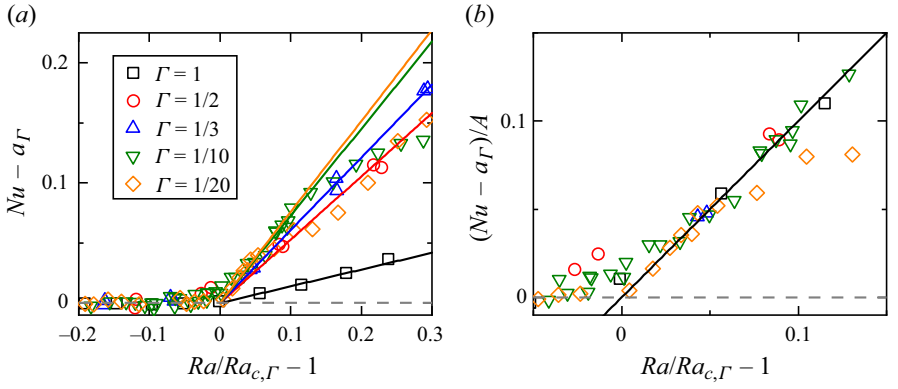

Figure 4. Experimentally obtained heat transport just above the onset of convection. (*a*) Here, $Nu - a_\Gamma$ versus $Ra/Ra_{c,\Gamma} - 1$. The horizontal dashed line marks the conduction state. The solid lines are linear fitting to the data just above the onset of convection, i.e. $Nu - a_\Gamma = A(Ra/Ra_{c,\Gamma} - 1)$. (*b*) Here, $(Nu - a_\Gamma)/A$ versus $Ra/Ra_{c,\Gamma} - 1$.

The experimentally measured Nu just above the onset of convection is shown in figure 4(*a*,*b*). It can be seen that the data also follow the linear trend (the solid lines) with the slope of the linear fitting increasing with decreasing Γ. However, a noticeable difference between A obtained numerically and experimentally can be observed, see figure 3(*c*). The possible reason might be twofold. First, figure 3(*a*) shows that the range of the linear trend shortens as Γ decreases. For example, the linear growth range is within $0 < Ra/Ra_{c,\Gamma} - 1 < 0.05$ in a cell with $\Gamma = 1/5$ and it shortens to within $0 < Ra/Ra_{c,\Gamma} - 1 < 0.01$ in a cell with $\Gamma = 1/20$. The Nu data go below the linear trend with increasing Ra, resulting in lower A if one cannot make measurements very close to the onset. It is very difficult to make measurements very close to $Ra_{c,\Gamma}$ in cells with $\Gamma \leq 1/10$. Thus, the experimentally measured A in this range is underestimated. Secondly, to reduce Γ for fixed D in the experiment, we increased the cell height H. In this case, the Oberbeck–Boussinesq approximation may not hold in these slender geometries due to

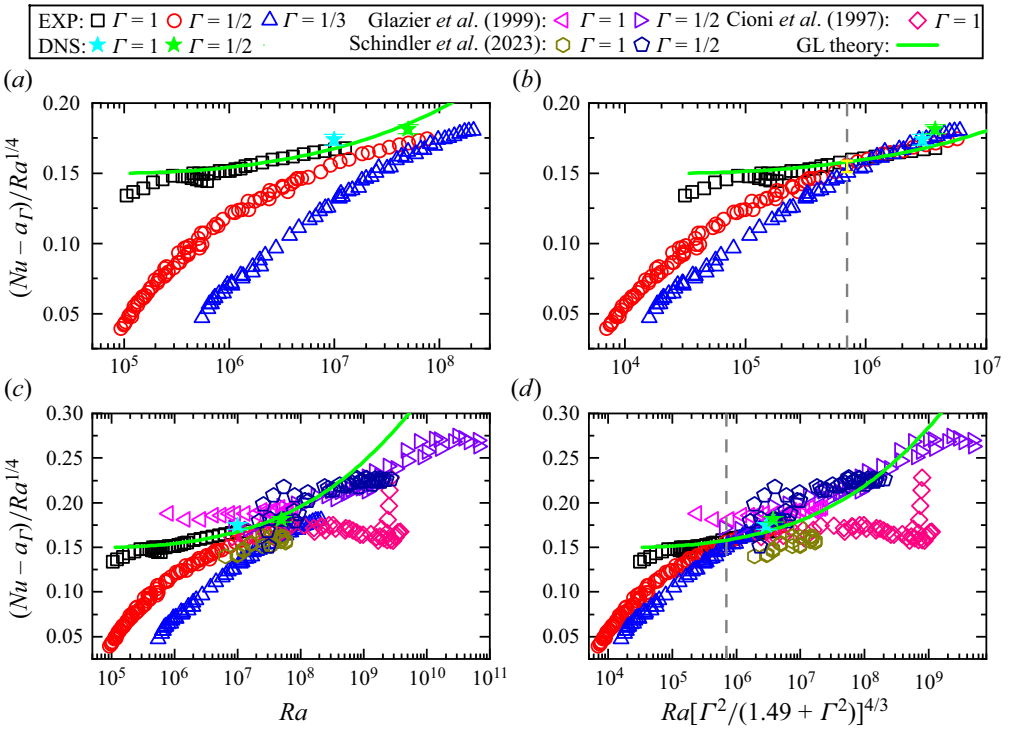

Figure 5. Data from the present study: (*a*) compensated plot of *Nu* versus *Ra* obtained experimentally (open symbols) and numerically (solid symbols) for different Γ; (*b*) compensated *Nu* versus Ra_ℓ, i.e. a Rayleigh number based on the length scale ℓ, for the same data as in (*a*). Comparison of the present data with those published in the literature: (*c*) compensated plot of *Nu* versus *Ra* and (*d*) compensated plot of *Nu* versus Ra_ℓ.

the pressure work that cannot be ignored in the energy equation (Shishkina 2021; Lohse & Shishkina 2024; Weiss, Emran & Shishkina 2024), which may also contribute to the difference between DNS and experiment.

The measured $Nu - a_\Gamma$ versus *Ra* in the turbulent state in cells with $\Gamma = 1$, $1/2$ and $1/3$ is shown as a compensated plot in figure 5(*a*). The green solid line marks the prediction of the GL theory in a $\Gamma = 1$ cell (Grossmann & Lohse 2000; Stevens *et al.* 2013). Although *Nu* in the $\Gamma = 1$ cell agrees well with the GL prediction, we see *Nu* data in cells with $\Gamma = 1/2$ and $1/3$ deviate from the $\Gamma = 1$ data and the GL prediction. As discussed previously, the appropriate length scale and Rayleigh number in turbulent liquid metal convection are $\ell = H/(1 + c_u\Gamma^{-2})^{4/9}$ and $Ra_\ell \equiv Ra/(1 + c_u\Gamma^{-2})^{4/3}$, respectively. Thus, we plot in figure 5(*b*) $(Nu - a_\Gamma)/Ra^{1/4}$ versus Ra_ℓ. It is seen that once Ra_ℓ is adopted, the *Nu* data collapse with each other and the GL prediction with the difference between them being smaller than 5 % for $Ra_\ell \geq 7 \times 10^5$, as indicated by the yellow error bar in figure 5(*b*). In addition, one observes that this difference in *Nu* decreases with increasing Ra_ℓ. We note that a similar collapse of *Nu* data with Ra_ℓ for different Γ is found in working fluids such as gas and water (with $\alpha = 1/3$) (Shishkina 2021; Ahlers *et al.* 2022). However, the functional form of ℓ and Ra_ℓ is different due to $Nu \sim Ra^{1/3}$ in these two fluids. We now test the proposed length scale in the turbulent state using data from the literature. Figure 5(*c*) plots $(Nu - a_\Gamma)/Ra^{1/4}$ versus *Ra* from present study and previous data in cells with $\Gamma = 1$ and 1/2 (Cioni *et al.* 1997; Glazier *et al.* 1999; Schindler *et al.* 2023). From figure 5(*c*), it can be seen that the overall trends of *Nu* versus *Ra* from different studies are

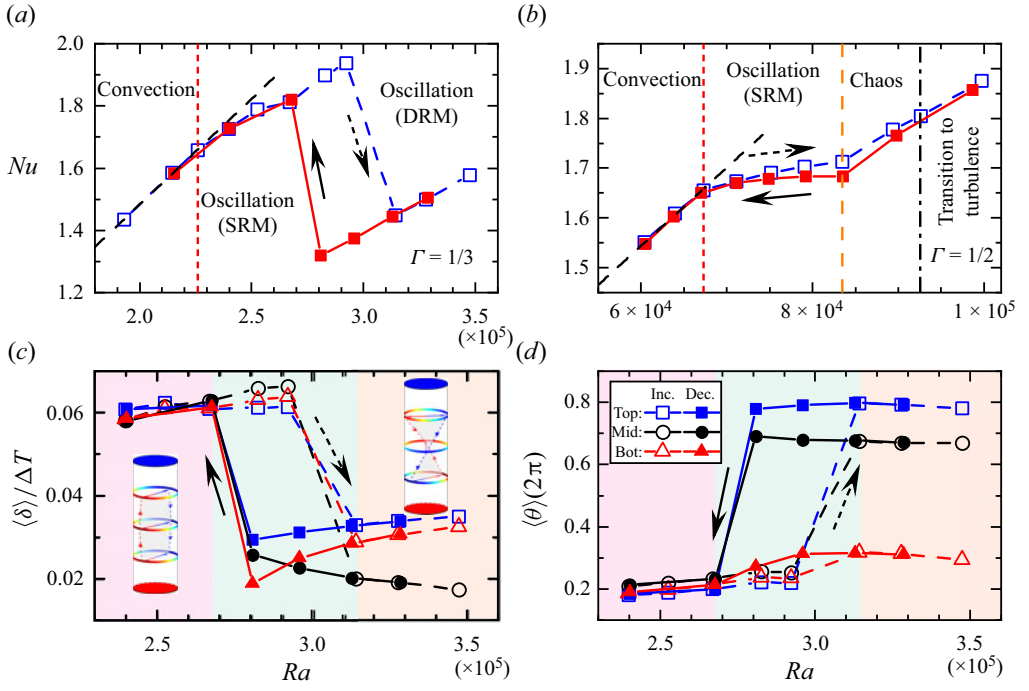

Figure 6. Here, Nu versus Ra for (*a*) $\Gamma = 1/3$ and (*b*) $\Gamma = 1/2$. The black dashed line represents a linear fitting to the Nu versus Ra data in the convection state. The vertical lines mark the transition between different flow states reported in Ren *et al.* (2024). Time averaged (*c*) flow strength $\langle\delta\rangle/\Delta T$ and (*d*) orientation $\langle\theta\rangle$ of the LSC versus Ra in the $\Gamma = 1/3$ cell. The open and solid symbols are taken with increasing and decreasing Ra, respectively. The lower left-hand and upper right-hand insets in (*c*) are reconstructed SRM and DRM from the sidewall temperatures.

consistent. When these Nu data are plotted against Ra_ℓ, as shown in figure 5(*d*), we notice that Nu data in cells with $\Gamma = 1/2$ will collapse on the prediction curve of GL theory with very weak Γ-dependence when $Ra_\ell \geq 7 \times 10^5$. One may notice that the data from Cioni *et al.* (1997) is systematically lower than the other groups of data, for which we do not know the exact reason. But it should be noted that different sidewall materials, i.e. stainless steel in Cioni *et al.* (1997) and Plexiglas in the present work, were used.

3.3. *The two discontinuities*

We now study the two discontinuities marked with rectangles in figure 2(*a*). Close-up views of the two rectangles are shown in figure 6(*a*,*b*) for $\Gamma = 1/3$ and $1/2$, respectively. Let us first focus on measurements in the $\Gamma = 1/3$ cell. With increasing Ra (open symbols in figure 6*a*), the system goes through a Hopf bifurcation, transitioning from the steady convection state to an oscillatory state (Ren *et al.* 2024). When time dependency occurs, we observe a drop in Nu, resulting in it not following the linear trend just above the onset of convection (the dashed line). Measurement of the LSC structure using the multi-thermal-probe method (Xie, Wei & Xia 2013) suggests that the LSC is a SRM in the convection state. This can be seen clearly from the time-averaged flow strength $\langle\delta\rangle$ and its orientation $\langle\theta\rangle$ shown as open symbols in figures 6(*c*) and 6(*d*), respectively. For $Ra < 2.68 \times 10^5$, typical behaviours for a single-roll LSC can be observed, i.e. δ at three heights with distances $H/4$, $H/2$ and $3H/4$ from the bottom plates remain close to each

other and well above zero; and $\langle\theta\rangle$ at three heights remains close to each other. A snapshot of the reconstructed SRM using the measured sidewall temperature is shown as an inset in the lower left-hand corner of figure 6(*c*). When *Ra* is increased beyond a critical point, i.e. 2.92×10^5, we observe a sudden drop of *Nu* up to 34 %. If we check $\langle\delta\rangle$ and $\langle\theta\rangle$ shown in figure 6(*c*,*d*), one sees that while $\langle\delta\rangle/\Delta T$ at the midheight of the cell drops close to zero, $\langle\delta\rangle/\Delta T$ at the top and bottom parts of the cell remains well above zero. Meanwhile, there is a $\sim \pi$ phase difference between the top and bottom parts of the LSC. These are typical signatures of a DRM of the LSC. The reconstructed structure of the DRM is shown in the upper right-hand corner of figure 6(*c*). It thus becomes clear that this sudden drop in *Nu* is due to a bifurcation of the LSC from the SRM to the DRM in the oscillation regime. When *Ra* is increased further, we only observe oscillation of this DRM. The bifurcation process discussed above is observed with increasing *Ra*. What will happen if we decrease *Ra*? In figure 6(*a*), the red solid squares are *Nu* measured when *Ra* is decreased from 3.92×10^5. Interestingly, the data shows hysteresis, i.e. the DRM could survive at even smaller *Ra* than the case with increasing *Ra*. In the convection state, we see no noticeable difference between increasing/decreasing *Ra*. The LSC is in the form of SRM.

Note the transition between SRM and DRM has been reported in Rayleigh–Bénard turbulence in water (Verzicco & Camussi 2003; Xi & Xia 2008; Weiss & Ahlers 2011). In addition, hysteresis between different flow structures is observed in Taylor–Couette turbulence (Huisman *et al.* 2014). The present study in liquid metal differs from that in water in two ways. Firstly, the heat transport difference in SRM and DRM in liquid metal is an order of magnitude larger than that in water. Secondly, the hysteresis is observed in an oscillation state, not a turbulent state.

In the $\Gamma = 1/2$ cell, we observed similar behaviours to that in the cell with $\Gamma = 1/3$ (cf. figure 6*b*). However, the LSC in this cell is always in the SRM. When a Hopf bifurcation occurs, we observe a slight drop in the linear slope of *Nu* versus *Ra*. In addition, hysteresis is observed when *Ra* is deceased. Because the structure of the LSC in this cell does not change, the maximum difference in *Nu* when hysteresis occurs is only 1.7 %.

The above observation indicates that when time dependency occurs in cells with $\Gamma = 1/2$ and 1/3, the heat transport of the system always decreases. If this time dependency could be delayed or even suppressed, e.g. by applying rotation or a magnetic field to liquid metal convection, one can then achieve higher heat transport efficiency, which will be useful in engineering heat transport management.

4. Conclusion

We have studied the effect of a small aspect ratio Γ on the heat transport in liquid metal convection with $Pr = 0.029$. In the range of $1/50 \leq \Gamma \leq 1$, the DNS shows that just above the onset of convection, $Nu - 1 = 0.018(1 + 0.34/\Gamma^2)(Ra/Ra_{c,\Gamma} - 1)$ which suggests that the relevant length scale ℓ is $\ell = H/(1 + c_u\Gamma^{-2})^{1/3}$ with $c_u = 1.49$. The local effective heat transport scaling exponent γ reaches its maximum before the system becomes turbulent. In a turbulent state, the measured value of γ approaches the GL prediction of 1/4 with increasing *Ra*. Assuming $Nu - 1 \sim Ra^\alpha$ in turbulent RBC, we propose that the length scales in cells with $\Gamma < 1$ is $\ell = H/(1 + c_u\Gamma^{-2})^{1/[3(1-\alpha)]}$. In the *Ra* range of the present study, we observe $\alpha = 0.25$ in turbulent liquid metal convection. Substituting $\alpha = 1/4$ into ℓ, one obtains a length scale $\ell = H/(1 + c_u\Gamma^{-2})^{4/9}$ and $Ra_\ell \equiv Ra/(1 + c_u\Gamma^{-2})^{4/3}$. Once the *Nu* is plotted against Ra_ℓ, the present study shows that, for $Ra_\ell \geq 7 \times 10^5$, the heat transport in cells with $1/3 \leq \Gamma \leq 1$ will collapse with

Case	$N_z \times N_\phi \times N_r$	Ra	Nu	Nu_{ϵ_u}	Nu_{ϵ_T}
$\Gamma = 1$	$512 \times 768 \times 256$	1.00×10^7	10.90	10.54	10.93
$\Gamma = 1/2$	$512 \times 512 \times 128$	5.00×10^7	16.34	15.94	16.45

Table 1. Details of the DNS in the turbulent state. Here Γ is the aspect ratio of the cell; N_z, N_ϕ and N_r are the number of grid points in the vertical, azimuthal and radial directions, respectively. Here Ra is the Rayleigh number; Nu, Nu_{ε_u} and Nu_{ε_T} are the directly calculated Nusselt number, the Nusselt number calculated based on the viscous dissipation rate and the thermal dissipation rate, respectively.

each other and with the prediction of the GL theory for $\Gamma = 1$. In turbulent thermal convection for $Pr > 1$ with $\alpha = 1/3$, the above proposed length scale ℓ replicates the justified length scale proposed by Shishkina (2021) and Ahlers *et al.* (2022), i.e. $\ell = H/(1 + c_u\Gamma^{-2})^{1/2}$. It is also found that when the flow transitions from a steady state to an oscillatory state with increasing Ra, the linear growth rate of Nu versus Ra declines. A hysteresis is observed in cells with $\Gamma = 1/3$ in the oscillation state. Measurements of the LSC suggest that the hysteresis is caused by the LSC switching from a SRM to a DRM. The SRM is found to be 34 % more efficient in heat transport when compared with that of the DRM. Since a reduced Γ for fixed D is always employed as an efficient way to achieve higher Ra, the present study demonstrates quantitatively how a decrease in Γ will affect the heat transport behaviour just above the onset of convection and in the turbulent state. It extends the recent theoretical findings by Shishkina (2021) obtained for moderate Pr to the case of liquid metal with small Pr. It will be interesting to test if Ra_ℓ is a proper control parameter for fluids with large Pr in the $\Gamma < 1$ regime and to turbulent liquid metal convection with even higher Ra where a transition to the ultimate regime is expected.

Acknowledgements. We are grateful to O. Shishkina for helpful discussions.

Funding. This work was supported by the National Science Foundation of China (grant nos 92152104, 12072144, 12232010, 12202173) and a XJTU young talent support plan.

Declaration of interests. The authors report no conflict of interest.

Author ORCIDs.
Lei Ren https://orcid.org/0000-0001-8256-0834;
Xin Tao https://orcid.org/0000-0002-7070-0788;
Lu Zhang https://orcid.org/0000-0003-4009-2969;
Ke-Qing Xia https://orcid.org/0000-0001-5093-9014;
Yi-Chao Xie https://orcid.org/0000-0002-2159-4579.

Appendix

Table 1 and table 2 provide details on the DNS.

https://doi.org/10.1017/jfm.2024.630 Published online by Cambridge University Press

Case	Ra	Nu	Nu_{ϵ_u}	Nu_{ϵ_T}	t_{all}	t_{sta}	Ra	Nu	Nu_{ϵ_u}	Nu_{ϵ_T}	t_{all}	t_{sta}
$\Gamma = 1$	3.70×10^3	1.0000	1.0000	1.0000	3000	2000	3.95×10^3	1.0016	1.0016	1.0016	3000	1000
$N_z = 24$	3.80×10^3	1.0000	1.0000	1.0000	3000	2000	3.97×10^3	1.0019	1.0018	1.0018	3000	1000
$N_\phi = 48$	3.90×10^3	1.0010	1.0010	1.0010	6000	2000	4.00×10^3	1.0023	1.0023	1.0023	3000	1000
$N_r = 12$	3.93×10^3	1.0013	1.0013	1.0013	3000	500	4.10×10^3	1.0038	1.0038	1.0038	3000	2000
$\Gamma = 1/2$	2.43×10^4	1.0006	1.0006	1.0006	9000	1500	2.50×10^4	1.0034	1.0034	1.0034	3000	1000
$N_z = 32$	2.44×10^4	1.0009	1.0009	1.0009	9000	3000	2.54×10^4	1.0052	1.0052	1.0052	3000	2000
$N_\phi = 32$	2.46×10^4	1.0017	1.0017	1.0017	6000	3000	2.56×10^4	1.0062	1.0061	1.0062	3000	2000
$N_r = 8$	2.48×10^4	1.0026	1.0025	1.0026	3000	1000	2.58×10^4	1.0072	1.0071	1.0072	3000	2000
$\Gamma = 1/3$	1.00×10^5	1.0000	1.0000	1.0000	3000	2000	1.07×10^5	1.0091	1.0089	1.0091	3000	1500
$N_z = 48$	1.04×10^5	1.0031	1.0030	1.0031	3000	500	1.08×10^5	1.0113	1.0110	1.0113	3000	2000
$N_\phi = 32$	1.05×10^5	1.0050	1.0049	1.0050	3000	1000	1.10×10^5	1.0159	1.0156	1.0159	3000	2000
$N_r = 8$	1.06×10^5	1.0070	1.0069	1.0070	3000	1500	1.13×10^5	1.0237	1.0232	1.0237	3000	2000
$\Gamma = 1/5$	7.20×10^5	1.0000	1.0000	1.0000	3000	2000	7.60×10^5	1.0241	1.0236	1.0241	3000	2000
$N_z = 80$	7.30×10^5	1.0046	1.0046	1.0046	6000	2000	7.70×10^5	1.0305	1.0299	1.0305	3000	2000
$N_\phi = 32$	7.40×10^5	1.0111	1.0109	1.0111	3000	1000	7.80×10^5	1.0331	1.0325	1.0331	3000	500
$N_r = 8$	7.50×10^5	1.0176	1.0173	1.0176	3000	1000	7.90×10^5	1.0364	1.0358	1.0364	6000	4000
$\Gamma = 1/10$	1.110×10^7	1.0000	1.0000	1.0000	10 000	4000	1.127×10^7	1.0135	1.0132	1.0135	10 000	5000
$N_z = 160$	1.120×10^7	1.0053	1.0052	1.0053	10 000	2000	1.130×10^7	1.0168	1.0165	1.0168	10 000	6000
$N_\phi = 32$	1.123×10^7	1.0087	1.0086	1.0087	10 000	4000	1.140×10^7	1.0245	1.0241	1.0245	10 000	3000
$N_r = 8$	1.125×10^7	1.0111	1.0109	1.0111	10 000	5000	1.150×10^7	1.0257	1.0252	1.0257	10 000	5000

Table 2. For caption see on next page.

https://doi.org/10.1017/jfm.2024.630 Published online by Cambridge University Press

Case	Ra	Nu	Nu_{ϵ_u}	Nu_{ϵ_T}	t_{all}	t_{sta}	Ra	Nu	Nu_{ϵ_u}	Nu_{ϵ_T}	t_{all}	t_{sta}
$\Gamma = 1/20$	1.760×10^8	1.0000	1.0000	1.0000	9000	3000	1.780×10^8	1.0189	1.0185	1.0189	24 000	14 000
$N_z = 320$	1.770×10^8	1.0012	1.0012	1.0012	62 200	7200	1.790×10^8	1.0276	1.0272	1.0277	24 000	9000
$N_\phi = 32$	1.773×10^8	1.0057	1.0056	1.0057	20 000	4000	1.800×10^8	1.0298	1.0293	1.0298	24 000	9000
$N_r = 8$	1.775×10^8	1.0091	1.0090	1.0091	15 000	3000	1.820×10^8	1.0334	1.0328	1.0334	10 833	4833
	1.777×10^8	1.0129	1.0126	1.0129	15 000	5000	1.840×10^8	1.0374	1.0368	1.0374	10 000	2000
$\Gamma = 1/40$	2.825×10^9	1.0107	1.0105	1.0107	51 149	11 149	2.833×10^9	1.0332	1.0327	1.0333	40 923	20 923
$N_z = 480$	2.826×10^9	1.0143	1.0141	1.0144	40 921	7921	2.835×10^9	1.0332	1.0327	1.0333	40 933	20 933
$N_\phi = 32$	2.827×10^9	1.0180	1.0177	1.0181	40 917	15 917	2.837×10^9	1.0334	1.0329	1.0335	40 943	25 943
$N_r = 8$	2.828×10^9	1.0217	1.0214	1.0218	40 915	17 915	2.840×10^9	1.0336	1.0330	1.0336	36 559	21 559
	2.830×10^9	1.0292	1.0288	1.0293	25 580	8580	2.850×10^9	1.0345	1.0339	1.0346	34 871	24 871
$\Gamma = 1/50$	6.893×10^9	1.0077	1.0076	1.0078	108 465	13 465	6.910×10^9	1.0363	1.0357	1.0364	53 677	18 677
$N_z = 640$	6.896×10^9	1.0141	1.0139	1.0142	64 928	9928	6.920×10^9	1.0348	1.0342	1.0348	48 679	28 679
$N_\phi = 32$	6.898×10^9	1.0184	1.0181	1.0184	63 032	13 032	6.930×10^9	1.0343	1.0338	1.0344	19 730	4730
$N_r = 8$	6.900×10^9	1.0226	1.0223	1.0227	44 533	8533	6.940×10^9	1.0346	1.0340	1.0346	19 740	4740

Table 2. Details of the DNS near the onset of convection in the range of $1/50 \leq \Gamma \leq 1$. The definitions of the symbols is the same as table 1. Only data very close to the onset of convection are listed. Note that a much longer simulation time is required in cells with smaller Γ to reach a statistically steady state.

References

Ahlers, G., *et al.* 2022 Aspect ratio dependence of heat transfer in a cylindrical Rayleigh–Bénard cell. *Phys. Rev. Lett.* **128**, 084501.

Ahlers, G., Grossmann, S. & Lohse, D. 2009 Heat transfer and large scale dynamics in turbulent Rayleigh–Bénard convection. *Rev. Mod. Phys.* **81**, 503–537.

Aurnou, J.M. & Olson, P.L. 2001 Experiments on Rayleigh–Bénard convection, magnetoconvection and rotating magnetoconvection in liquid gallium. *J. Fluid Mech.* **430**, 283–307.

Chen, X.-Y., Xie, Y.-C., Yang, J.-C. & Ni, M.-J. 2023 Strong coupling of flow structure and heat transport in liquid metal thermal convection. *J. Fluid Mech.* **975**, A21.

Chillá, F. & Schumacher, J. 2012 New perspectives in turbulent Rayleigh–Bénard convection. *Eur. Phys. J.* E **35**, 58.

Chong, K.-L., Ding, G.-Y. & Xia, K.-Q. 2018 Multiple-resolution scheme in finite-volume code for active or passive scalar turbulence. *J. Comput. Phys.* **375**, 1045–1058.

Cioni, S., Ciliberto, S. & Sommeria, J. 1997 Strongly turbulent Rayleigh–Bénard convection in mercury: comparison with results at moderate Prandtl number. *J. Fluid Mech.* **335**, 111–140.

Frick, P., Khalilov, R., Kolesnichenko, I., Mamykin, A., Pakholkov, V., Pavlinov, A. & Rogozhkin, S. 2015 Turbulent convective heat transfer in a long cylinder with liquid sodium. *Europhys. Lett.* **109**, 14002.

Glazier, J.A., Segawa, T., Naert, A. & Sano, M. 1999 Evidence against 'ultrahard' thermal turbulence at very high Rayleigh numbers. *Nature* **398**, 307–310.

Grossmann, S. & Lohse, D. 2000 Scaling in thermal convection: a unifying theory. *J. Fluid Mech.* **407**, 27–56.

Horanyi, S., Krebs, L. & Müller, U. 1999 Turbulent Rayleigh–Bénard convection in low Prandtl-number fluids. *Intl J. Heat Mass Transfer* **42**, 3983–4003.

Huang, S.-D., Kaczorowski, M., Ni, R. & Xia, K.-Q. 2013 Confinement-induced heat-transport enhancement in turbulent thermal convection. *Phys. Rev. Lett.* **111**, 104501.

Huisman, S.G., van der Veen, R.C., Sun, C. & Lohse, D. 2014 Multiple states in highly turbulent Taylor–Couette flow. *Nat. Commun.* **5**, 3820.

King, E.M. & Aurnou, J.M. 2013 Turbulent convection in liquid metal with and without rotation. *Proc. Natl Acad. Sci.* **110**, 6688–6693.

Lohse, D. & Shishkina, O. 2023 Ultimate turbulent thermal convection. *Phys. Today* **76**, 26–32.

Lohse, D. & Shishkina, O. 2024 Ultimate Rayleigh–Bénard turbulence. *Rev. Mod. Phys.* **96**, 035001.

Lohse, D. & Xia, K.-Q. 2010 Small-scale properties of turbulent Rayleigh–Bénard convection. *Annu. Rev. Fluid Mech.* **42**, 335–364.

Mamykin, A., Frick, P., Khalilov, R., Kolesnichenko, I., Pakholkov, V., Rogozhkin, S. & Vasiliev, A. 2015 Turbulent convective heat transfer in an inclined tube with liquid sodium. *Magnetohydrodynamics* **51**, 329–336.

Ren, L., Tao, X., Xia, K.-Q. & Xie, Y.-C. 2024 Transition to fully developed turbulence in liquid–metal convection facilitated by spatial confinement. *J. Fluid Mech.* **981**, R2.

Ren, L., Tao, X., Zhang, L., Ni, M.-J., Xia, K.-Q. & Xie, Y.-C. 2022 Flow states and heat transport in liquid metal convection. *J. Fluid Mech.* **951**, R1.

Rossby, H.T. 1969 A study of Bénard convection with and without rotation. *J. Fluid Mech.* **36**, 309–335.

Salavy, J.F., Boccaccini, L.V., Lässer, R., Meyder, R., Neuberger, H., Poitevin, Y., Rampal, G., Rigal, E., Zmitko, M. & Aiello, A. 2007 Overview of the last progresses for the European Test Blanket Modules projects. *Fusion Engng Des.* **82**, 2105–2112.

Scheel, J.D. & Schumacher, J. 2016 Global and local statistics in turbulent convection at low Prandtl numbers. *J. Fluid Mech.* **802**, 147–173.

Schindler, F., Eckert, S., Zürner, T., Schumacher, J. & Vogt, T. 2022 Collapse of coherent large scale flow in strongly turbulent liquid metal convection. *Phys. Rev. Lett.* **128**, 164501.

Schindler, F., Eckert, S., Zürner, T., Schumacher, J. & Vogt, T. 2023 Erratum: collapse of coherent large scale flow in strongly turbulent liquid metal convection. *Phys. Rev. Lett.* **131**, 159901.

Shishkina, O. 2021 Rayleigh–Bénard convection: the container shape matters. *Phys. Rev. Fluids* **6**, 090502.

Stevens, R.J.A.M., van der Poel, E.P., Grossmann, S. & Lohse, D. 2013 The unifying theory of scaling in thermal convection: the updated prefactors. *J. Fluid Mech.* **730**, 295–308.

Takeshita, T., Segawa, T., Glazier, J.A. & Sano, M. 1996 Thermal turbulence in mercury. *Phys. Rev. Lett.* **76**, 1465–1468.

Van der Poel, E.P., Stevens, R.J.A.M. & Lohse, D. 2011 Connecting flow structures and heat flux in turbulent Rayleigh–Bénard convection. *Phys. Rev.* E **84**, 045303.

VERZICCO, R. 2004 Effects of nonperfect thermal sources in turbulent thermal convection. *Phys. Fluids* **16**, 1965–1979.

VERZICCO, R. & CAMUSSI, R. 1997 Transitional regimes of low-Prandtl thermal convection in a cylindrical cell. *Phys. Fluids* **9**, 1287–1295.

VERZICCO, R. & CAMUSSI, R 2003 Numerical experiments on strongly turbulent thermal convection in a slender cylindrical cell. *J. Fluid Mech.* **477**, 19–49.

WEISS, S. & AHLERS, G. 2011 Turbulent Rayleigh–Bénard convection in a cylindrical container with aspect ratio $\Gamma = 0.50$ and Prandtl number $Pr = 4.38$. *J. Fluid Mech.* **676**, 5–40.

WEISS, S., EMRAN, M.S. & SHISHKINA, O. 2024 What Rayleigh numbers are achievable under Oberbeck–Boussinesq conditions? *J. Fluid Mech.* **986**, R2.

XI, H.-D. & XIA, K.-Q. 2008 Flow mode transitions in turbulent thermal convection. *Phys. Fluids* **20**, 055104.

XIA, K.-Q. 2013 Current trends and future directions in turbulent thermal convection. *Theor. Appl. Mech. Lett.* **3**, 052001.

XIA, K.-Q., HUANG, S.-D., XIE, Y.-C. & ZHANG, L. 2023 Tuning heat transport via coherent structure manipulation: recent advances in thermal turbulence. *Nat. Sci. Rev.* **10**, nwad012.

XIE, Y.-C., WEI, P. & XIA, K.-Q. 2013 Dynamics of the large-scale circulation in high-Prandtl-number turbulent thermal convection. *J. Fluid Mech.* **717**, 322–346.

ZHANG, L. & XIA, K.-Q. 2023 Heat transfer in a quasi-one-dimensional Rayleigh–Bénard convection cell. *J. Fluid Mech.* **973**, R5.

ZÜRNER, T., SCHINDLER, F., VOGT, T., ECKERT, S. & SCHUMACHER, J. 2019 Combined measurement of velocity and temperature in liquid metal convection. *J. Fluid Mech.* **876**, 1108–1128.